\$ SUPER

Contents lists available at ScienceDirect

Materials Characterization

journal homepage: www.elsevier.com/locate/matchar





Evolution of microstructure and strength during accumulative extrusion bonding of multilayered copper tubes

Matthew R. Standley, Md. Zahidul Sarkar, Ethan E. Costa, Marko Knezevic *

Department of Mechanical Engineering, University of New Hampshire, Durham, NH 03824, USA

ARTICLE INFO

Keywords:
Microstructures
Strength
Metallic tubes
Accumulative extrusion bonding
Crystal plasticity

ABSTRACT

Accumulative extrusion bonding (AEB) was recently conceived as a novel severe plastic deformation (SPD) process to steady-state bond metals in the pursuit of manufacturing ultrafine-laminated bimetallic tubes. In a recent publication, we have reported details pertaining to the AEB process as uniquely suited to produce geometrical shapes such as tubes. The process has been successfully applied to extrusion bond a Cu-Cu bimetallic tube at room temperature. The bonding was facilitated under about 68% radial strain, which is more than required for accumulative roll bonding (ARB) of the same material. In this paper, we present the main results from an experimental investigation into the evolution of interface crystallography and integrity, grain structure, crystallographic texture, and tensile strength of the Cu—Cu tube. While the interface maintains overall integrity, it exhibits wavy character locally due to grain-scale plasticity. These observations suggest that laminated structures could be achieved with the continuation of the process. Characterization of grain orientations on each side of the bond line reveals that bonding using AEB at room temperature produces a steady-state bond independent on preferential grain orientations. Grains become severely elongated along the extrusion direction, while texture forms a moderately strong {111} fiber during the process. A crystal plasticity simulation of texture evolution during the process reveals minor gradients in the texture over the through-thickness direction. Predicted fields of strain during the process show that texture evolution is a consequence of not only large axial strain along the extrusion direction but also severe radial reduction and some shear strain. As a result of large microstructural changes, yield strength of the Cu—Cu tube remarkably increases over $5\times$ in the axial direction relative to the annealed material.

1. Introduction

Improving material properties is typically accomplished by alloying to promote solid solution strengthening and by controlling precipitation and recrystallization through heat treatments to achieve phase and grain structure distributions [1–3]. An approach used mainly for steels entails discovering a compromise between strength and ductility using a mixture of phases achieved by alloying and heat treatments [4–7]. Alternatively, in aluminum alloys, an aging treatment is required to provide the strength by precipitation hardening [8–10]. Beyond these options, a selected manufacturing process can influence material properties. This occurs as the grain structure and texture evolve due to strain fields necessary to form metals into their desired geometrical shapes. To this end, scalable manufacturing processes that produce ultrafine grains (UFGs) promoting strength continue to be on the forefront of research,

as the underlying mechanisms are investigated to predict and optimize material properties. The increase in strength of UFGs materials is owing to refined grain structure described by Hall and Petch [11,12] and underlying dislocation substructures [13]. Many manufacturing processes, which impose severe plastic deformation (SPD), have been developed in the modern era to produce UFGs. These processes have been utilized to produce shapes such as sheet, plates, and bars. Examples of such processes include equal channel angular pressing (ECAP) [14], high pressure torsion (HPT) [15], high pressure double torsion (HPDT) [16–20], accumulative roll bonding (ARB) [21–24], cyclic extrusion compression (CEC) [25], and accumulative extrusion bonding (AEB) [26,27]. In any of these processes, an initial grain structure is refined, while the strength is enhanced [28,29]. In addition, SPD techniques like ARB can be utilized to produce laminated bimetals to improve ballistic energy absorption [30], thermal stability and tolerance to radiation damage [31]

E-mail address: marko.knezevic@unh.edu (M. Knezevic).

^{*} Corresponding author at: Department of Mechanical Engineering, University of New Hampshire, 33 Academic Way, Kingsbury Hall, W119, Durham, NH, 03824, USA.

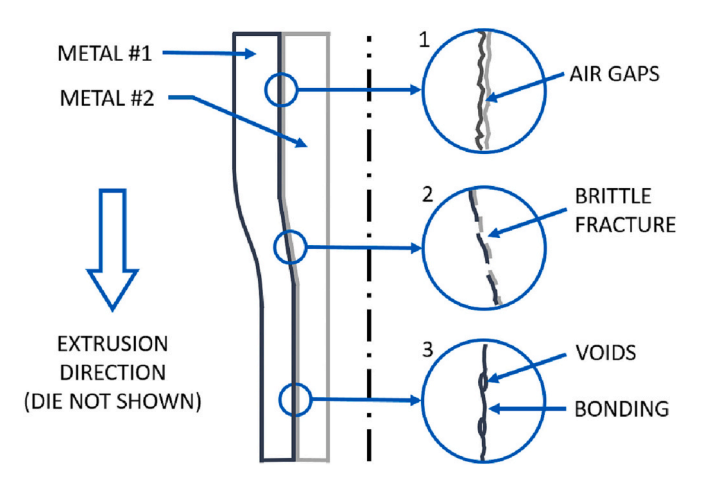


Fig. 1. Axis-symmetric cross section of the tubular extrusion process. Shown are the three stages of bonding during AEB: initial contact, ultra-high pressure, and exit/bonding. The die, punch, and mandrel are omitted.

in addition to improved hardness, yield strength, and ultimate tensile strength [32–34].

Obtaining refined grains in geometrical shapes such as metallic tubes by creating bimetallic tubing has been recently attempted using AEB in [35]. A broad set of manufacturing parameters needed to be considered to achieve bonding of similar or dissimilar metals, while producing UFGs in tubes. The set of parameters included the extrusion die angle, material selection, lubrication, extrusion speed, and material preparation [36–38]. The work in [35] primarily focused on bonding of a monometallic material. As a result, a few critical parameters did not need consideration such as the dissimilarity of yield stress. Ratios of yield stress greater than 3.5, for example, are not recommended as global fracture can occur during forming [36]. In addition, differences in atomic packing did not influence the bonding process since metals had the same atomic structure. Additionally, oxidation layers on both metal interfaces were consistent in terms of thickness and cohesion, and thereby this influence was also mitigated. This has been studied in other research [39], which has shown various oxide layer thicknesses dramatically influence peel strength between bonded specimens.

The AEB process was successfully optimized to extrusion bond a 99.95% commercially pure face-centered cubic (FCC) copper-copper (Cu—Cu) bimetallic tube at room temperature [35]. The bonding was facilitated under about 68% radial strain. Notably, bonding did not occur when extruding at 50% deformation, which typically produced

bonding in ARB as reported in [40–42]. The more complex geometry of tubes influenced the mechanical fields and higher levels of strain were required to enact bonding using AEB [35]. Successful bonding using ARB is well documented for a variety of different metal combinations in plate form such as Al/Cu [43], Cu/Ti [40], Mg/Al [44], Al/Zn [41], Cu/Zn [42], Cu/Zn/Al [45], Mg/Nb [46], Zr/Nb [47,48], and Zn/Sn [49]. When the layering is refined to the sub-micron and nanometer scale, the multilayered bimetallic sheets exhibit significantly improved strength [32,33], resistance to shock damage [50], thermal stability [51,52], and resistance to radiation damage [53,54]. Creating such layered structures in tubing remains somewhat illusive for the time being and is left for future works.

The present work is concerned with an experimental characterization of the evolution of interface crystallography and integrity, grain structure, crystallographic texture, and strength of the successfully bonded Cu—Cu tube. Understanding the bonding of the first extrusion pass is deemed critical as bonding must occur during the first extrusion pass for future extrusion iterations to successfully bond in AEB. The characterization is performed using optical microscopy, scanning electron microscopy (SEM) fitted with an electron backscatter diffraction (EBSD) camera, and standard mechanical testing. The study is the first report into the formation of microstructure in tubes during AEB. In addition, a finite element (FE) simulation of the process was performed using an elasto-plastic self-consistent (EPSC) polycrystal model coupled with FE software Abaqus to predict and discuss texture evolution during the process.

2. Methods

2.1. Theory of bonding

Bonding occurs at the adjoining interface as described by the thin film theory [55–58], which prevails over other proposed theories. Other bonding mechanisms have been proposed but nearly all ARB and AEB research points to the necessity to scratch brush, which creates the thin brittle film, and high pressure. Both are hallmarks of the thin film theory. Other theories include overcoming energy barriers [59,60], diffusion [61], and joint recrystallization [62]. The thin film theory is depicted schematically in Fig. 1 and is briefly described in the steps below (the step numbers correlate to the numbers in the figure).

 Preparation: A very thin brittle surface must exist on both metallic interfaces. An air gap exists between the adjoining metals. The interface must be clean to avoid inclusions.

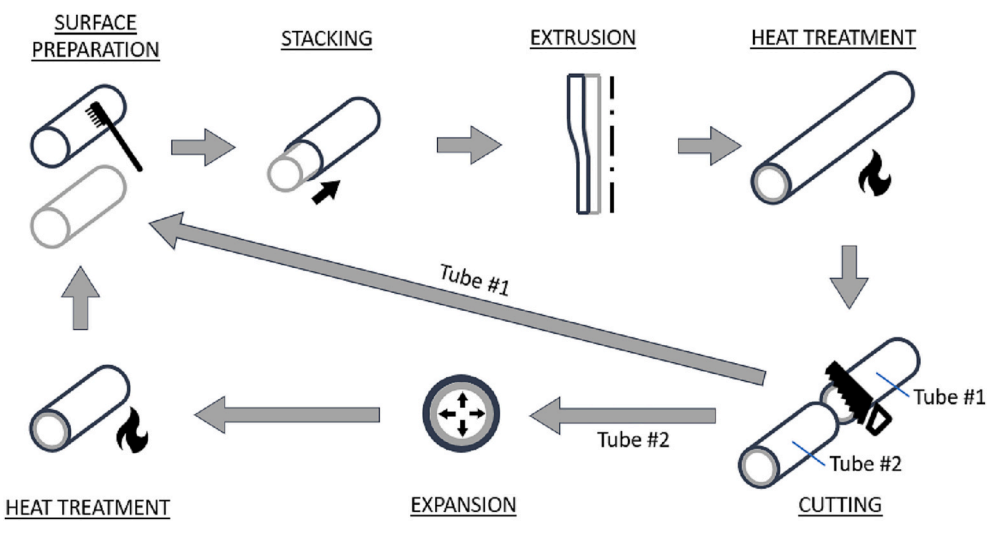


Fig. 2. The manufacturing process for achieving ultrafine-laminated structures in bimetallic tubes using AEB.

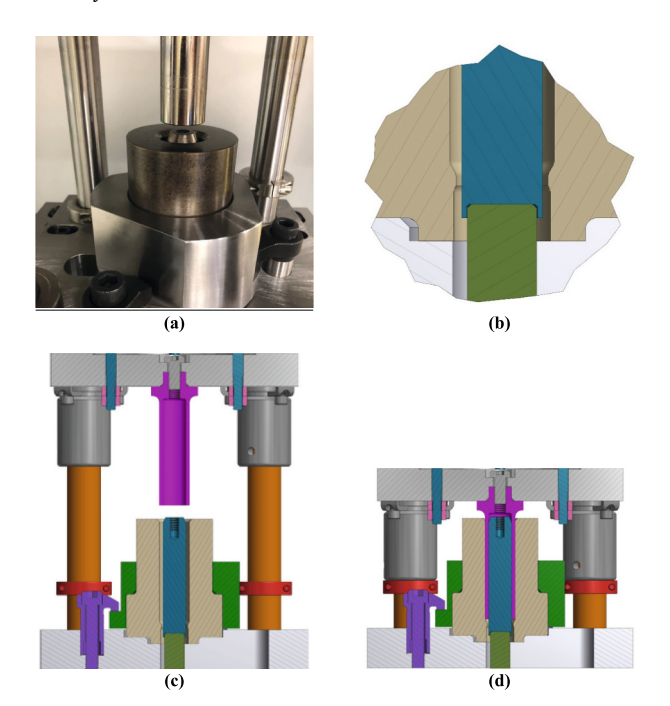


Fig. 3. (a) The experimental setup mounted in a hydraulic press, (b) a cross-sectional view of the extrusion die, and the punch located at the (c) initial and (d) final positions.

- 2. <u>Ultra-high pressure</u>: The metallic faces are forced into one interface, where the brittle surfaces crack under the high pressure induced by strain caused by a die and punch. The air gap is effectively removed and rendered to small local areas.
- 3. <u>Bonding</u>: Fresh non-oxidated virgin material passes through the cracks and interacts with the opposing virgin material to form a metallic bond. Some areas may not bond, and small local voids may become present.

2.2. AEB procedure

Multilayered bimetallic tubing is envisioned to be manufactured in an iterative AEB process to achieve a thin alternating lamented microstructure with UFGs. The process is iterated until the desired lamented thickness is achieved and is shown schematically in Fig. 2. The nominal layers within the tube wall exponentially decreases per $n=2^i$, where n represents the number of layers and i is the iteration.

Table 1
Hardening law parameters for Cu.

| Parameter | Value | Unit |
|-----------|-------|-------------------|
| $	au_0$ | 15 | MPa |
| k_1 | 3.5e7 | m^{-1} |
| g | 0.09 | _ |
| D | 40 | MPa |

For extrusion bonding, the two initially annealed metals are prepared by scratch brushing, are stacked, and then extruded. After extrusion, the bimetal is annealed and bisected. One of the bisected tubes is then expanded, annealed again, and the process starts over. The process steps are described below [35]. For the scope of research discussed herein, the metals only received surface preparation, stacking, and extrusion, but for completeness, the remaining processing steps planned in future works are also described.

- 1. Surface preparation: As a critical step, the joining surfaces are prepared by acid cleaning, acetone cleaning, and scratch brushing with a stainless-steel brush. The cleaning is done by dipping in a solution of 10% sulfuric acid and 90% distilled water per volume. After neutralizing in cool distilled water, the copper is further degreased in an ultrasonic acetone bath for 30 min, where the acetone is drained and replenished halfway through the cleaning process. After cleaning, the surface is prepared by scratch brushing. Scratch brushing is applied lightly and perpendicular to the extrusion direction. The intent is to promote the largest crack openings, which should occur when scratches are oriented normal to the direction of primary strain.
- Stacking: This operation is the simple action of inserting one tube into another. As described in other research [63], it is desired to assemble and extrude within 2 min or ideally in the least possible time to minimize the regrowth of surface oxidation. A slip fit of 0.05 mm is utilized.
- 3. Extrusion: SPD is produced using a die, mandrel, and punch as shown in Fig. 3. The die design is based on previous research [37], which was improved in subsequent research [35]. Extrusion was enacted at 68% deformation by maintaining the inner diameter and reducing the outer diameter. The die entrance measures 28.70 mm in diameter, where the inner mandrel is 22.07 mm. The diameter at the extrusion ledge reduces to 24.18 mm at a 30-degree taper. Extrusion was performed at 2.73 mm/s, where the die and mandrel were lubricated with non-diluted Drawsol WM 4740.

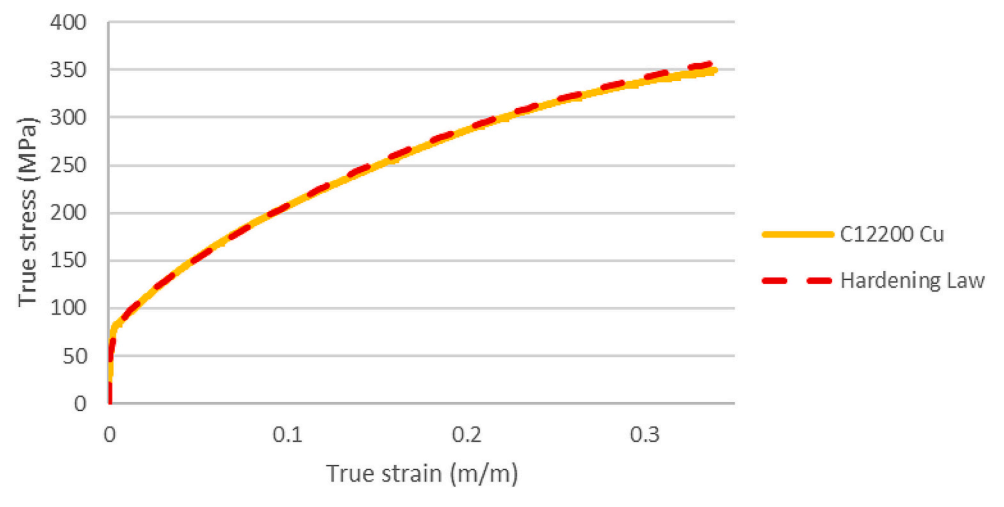


Fig. 4. Measured and simulated true stress-strain curves of annealed copper.

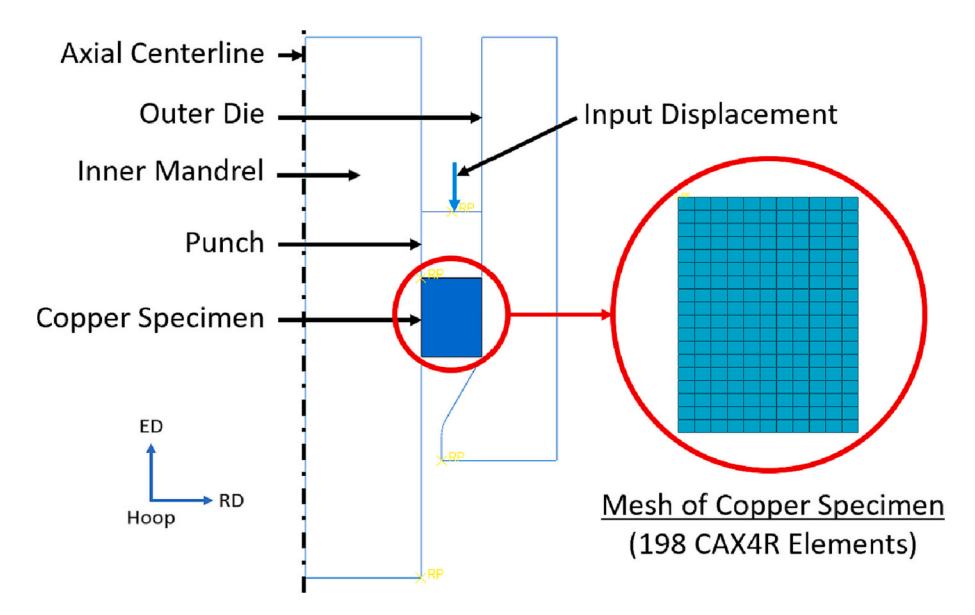


Fig. 5. Finite element geometry of the extrusion process modeled in ABAQUS to predict expected texture. Model is 2-dimensional and axisymmetric about the left edge, which is the centerline of the extrusion process.

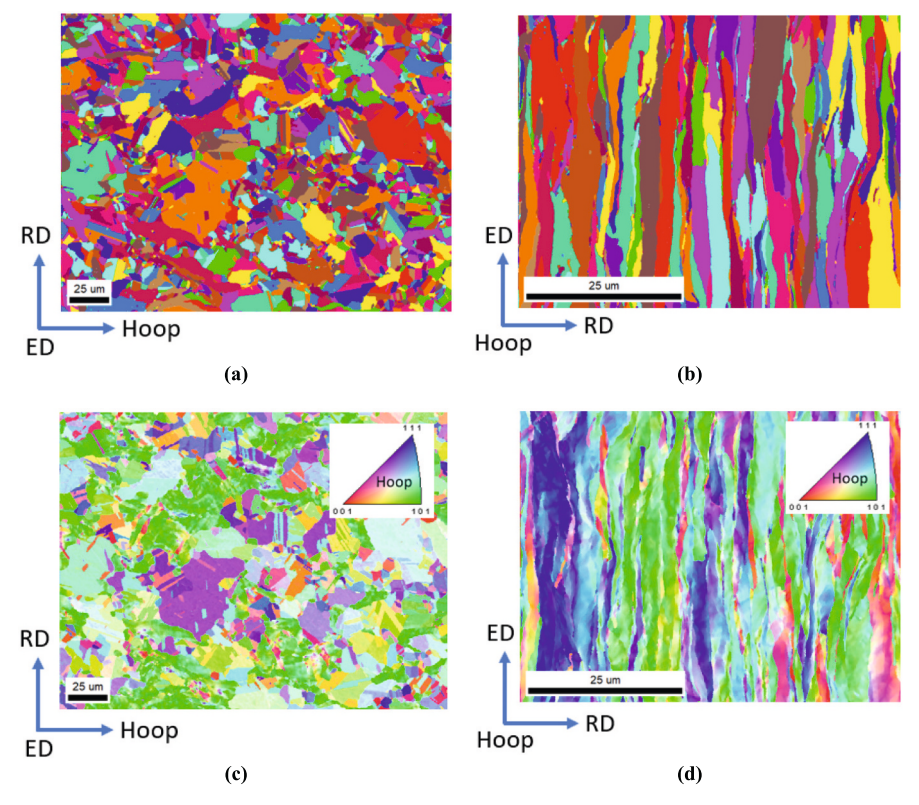


Fig. 6. (a) A grains map of the annealed pre-extruded Cu and (b) a grain map of the post-extruded Cu scanned using EBSD. Corresponding IPF maps (c, d).

- 4. <u>Cutting</u>: The extruded tube is bisected perpendicular to the axial centerline.
- 5. Expansion: Expansion is performed using a 10° tapered mandrel. The bimetal tube is passed multiple times to remove spring-back.
- 6. Heat treatment: The tubes are annealed after every SPD process in a vacuum oven at 426 $^{\circ}$ C with a 1 h soak and cooled at a rate of 426 $^{\circ}$ C/h. This heat treatment was utilized for the initial annealing of the asreceived copper, as well as for the intermediate annealing as shown in Fig. 2.

2.3. Material

The initial Cu material was a C12200 grade seamless tube per ASTM B75–20 (required a minimum purity of 99.95%). The commercially available tubes were procured with an outer diameter of 28.58 and 25.40 mm, both with a 1.65 mm wall thickness. The inner tube was machined to create a 0.05 mm slip fit with the outer tube. Based on ASTM E8–21, the true stress-strain curve of the material is presented in Fig. 4 after initial annealing was performed. The annealing, utilized to remove the as-procured temper of H58, was performed at 426 $^{\circ}\text{C}$ with a

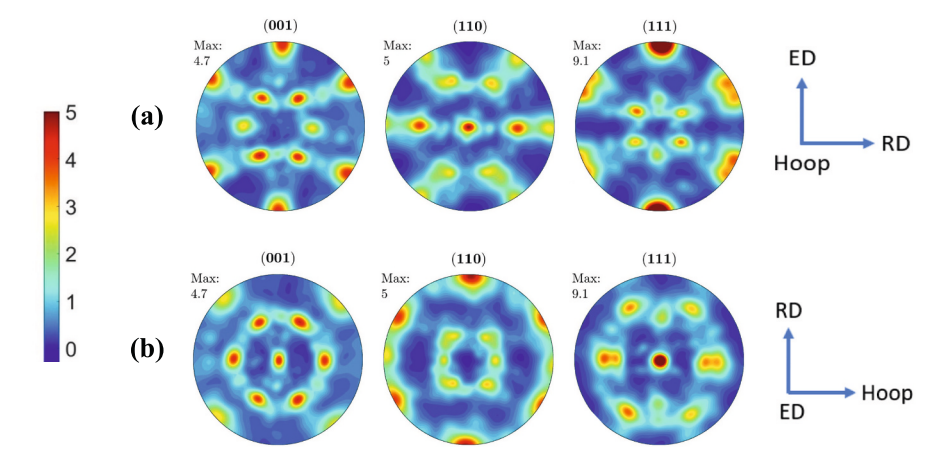


Fig. 7. Texture of the initially annealed copper, as measured using EBSD, utilized for predicting texture in the post-extruded state using EPSC FEA modeling at 68% deformation. Texture is presented in both the (a) hoop and (b) extrusion direction.

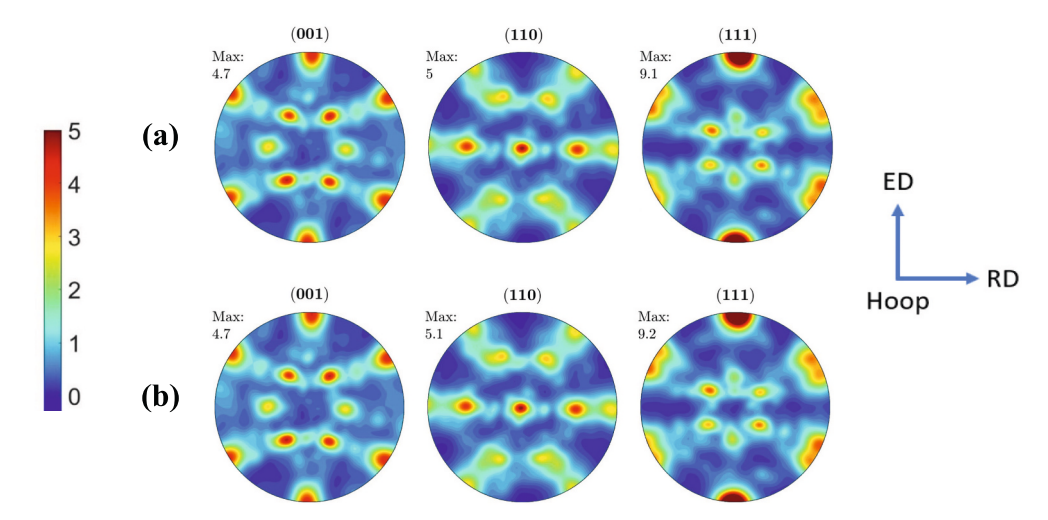


Fig. 8. (a) Initial texture, as measured using EBSD before extrusion, and (b) the compaction of the same data set to 100 representative grains.

 $1\,$ h soak time as recommended per [64]. Restored ductility was confirmed based on comparing the microhardness before and after annealing. The hardness after annealing was found to be 56.1 HK based on averaging the results of 10 hardness tests using a 500 g force held for 10 to 15 s. This represents a $\sim 60\%$ reduction in hardness.

As shown in Fig. 4, the experimental curve is simulated using EPSC and underlying dislocation density-based hardening law implemented in it. The model was presented in earlier works [65–67]. Only the main equations pertaining to the hardening law are presented here to appreciate the calibrated parameters for Cu established in this work. The parameters are tabulated in Table 1. The established parameters of the model are used to simulate the extrusion process and underlying texture evolution using an FE implementation of the EPSC model (FE-EPSC), which is written as a sub-routine for ABAQUS Version 2020 [68–70].

In the hardening law, the slip resistance of individual slip systems, τ_c^s , evolves from an initial value, τ_0 , using [71–74].

$$\tau_c^s = \tau_0 + \tau_{forest}^s \tag{1}$$

where, τ_{forest}^s is the slip resistance contribution originating from the build up of forest dislocations. The τ_{forest}^s evolves using [75–77].

$$\tau_{forest}^{s} = b\chi\mu\sqrt{\sum_{s}\rho_{for}^{s}}$$
 (2)

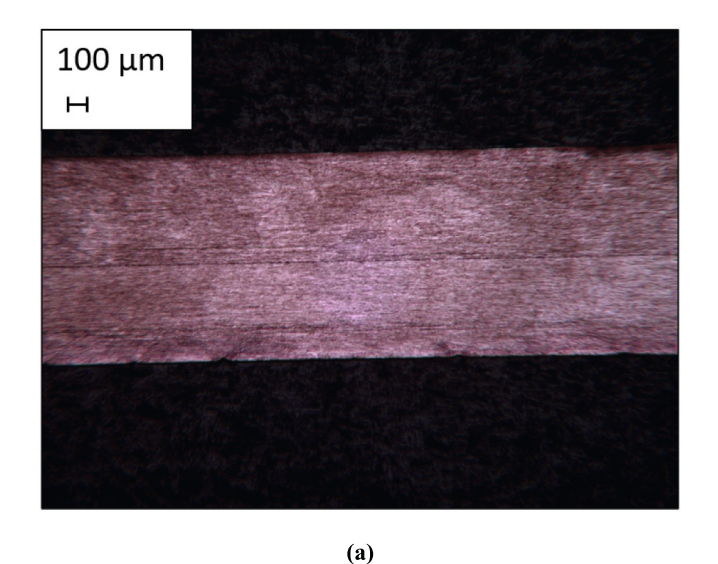
where, b is the Burgers vector for Cu, 2.556×10^{-10} m, χ is a dislocation interaction constant taken as 0.9, μ is the shear modulus calculated using the crystal elastic constants for Cu, $C_{11}=168.4$ GPa, $C_{12}=121.4$ GPa, and $C_{44}=75.4$ GPa, and ρ_{for}^s is the accumulated forest density of dislocations per s^{th} slip system. The increase of accumulated dislocation density with plastic strain is governed by a competition between the rate of generation and the rate of recovery using [78–81].

$$\frac{\partial \rho_{for}^s}{\partial r^s} = k_1 \sqrt{\rho_{for}^s} - k_2(\dot{\varepsilon}, T) \rho_{for}^s \tag{3}$$

Here, the rate coefficient of trapping k_1 is a calibration constant, while the rate coefficient of recovery k_2 is based on [82–84].

$$\frac{k_2}{k_1} = \frac{\chi b}{g} \left(1 - \frac{k_B T}{D(b)^3} ln \left(\frac{\dot{\varepsilon}}{\dot{\varepsilon}_0} \right) \right) \tag{4}$$

where, k_B and $\dot{\varepsilon}_0$ are the Boltzmann constant and a reference strain rate of value 10^7 s⁻¹. Two additional calibration constants are g and D. These are an effective activation enthalpy and a drag stress. The slip in the model is carried out using $\{111\}\langle 1\overline{1}0\rangle$ slip family.



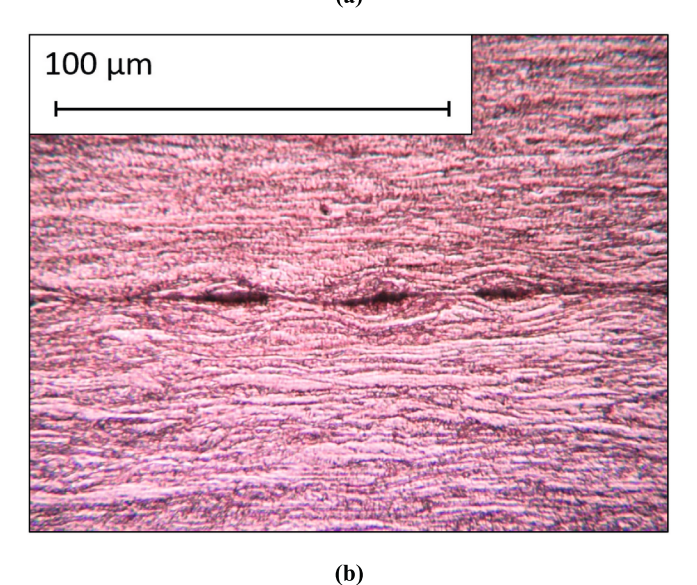


Fig. 9. (a) A micrograph showing a section of the as extruded 2-layer Cu—Cu tube. (b) A magnified view showing voids along the interface of 2-layer Cu—Cu tube shown.

2.4. Characterization of structures

Texture evolution is determined by measuring the texture before and after extrusion using EBSD. The samples were mounted in epoxy, ground, and polished using progressively finer sanding papers, and then finished with 30 min of vibratory polishing using 0.04 µm colloidal silica suspension. A pre-extrusion sample was mounted normal to the tube axis, while a post-extrusion sample was mounted normal to the hoop direction. In post-processing, textures and inverse pole figures (IPFs) were rotated appropriately to configure coordinate systems consistently.

The SEM used for the study is a Lyra3 focused ion beam electron microscope manufactured by Tescan. The EBSD detector is a Hikari series camera manufactured by AMETEK EDAX, which utilizes EDAX TEAM $^{\rm TM}$ software. For all EBSD maps collected, an average confidence index (CI) was found to be in the range of 0.81–0.84 for all scans, with points less than 0.1 cleaned-up automatically using EDAX OIM Analysis $^{\rm TM}$ 8 software. CI cleaning represented 6.0% and 4.1% of the total points for the pre- and post-extrusion samples, respectively. Scans were performed at 15.1 kV with a spot size of 38 and 46 nm and maps were collected at a step size of 0.3 and 0.1 μm for the pre- and post-extrusion samples, respectively. Lastly, texture data was calculated based on 3

scans of the pre-extrusion sample, where $\sim\!\!10,\!000$ grains were identified, and 6 scans of the post-extrusion sample, where $\sim\!\!3000$ grains were identified. The scans of the pre-extruded sample were collected at the midpoint within the tube wall and the post-extrusion sample was collected 0.25 mm from the outer tube. This distance places the scan location at the midpoint of the outer bonded tube.

Texture evolution is predicted using the FE-EPSC polycrystal model and compared with the measurements at the given location. The inputs to the FE-EPSC model was the pre-extrusion texture data, the die geometry, and the set of calibrated parameters for Cu. Lastly, all texture plots were created using MATLAB 2022a and custom codes written utilizing the MTEX 5.4.0 toolbox.

2.5. Finite element analysis – setup for simulation of extrusion

The extrusion process, as shown in Fig. 3, is modeled in ABAQUS 2D to gain insight on texture evolution. The geometry of the FEA model consists of the bottom portion of the inner mandrel, the outer die, and the copper specimen experiencing extrusion as shown in Fig. 5. Also shown is the coordinate axis definition, where the extrusion direction (ED) is aligned vertically, the radial direction (RD) extends outward from the vertical centerline, and the hoop direction is normal to the ED-RD plane. The analysis is simplified as 2-dimensional and axisymmetric since the extrusion die self-centers when used and since no 3-dimensional irregularities in stress or strain are expected due to processing as an extrusion [35]. Additionally, the die and mandrel are simplified as perfectly rigid since the stresses and strain in the fixturing are not of interest and since any influence of the die straining has a negligible influence on texture evolution.

The model is meshed with CAX4R type elements, which are 2-dimensional 4-node quadrilateral elements. After performing a mesh density study, the model contains 198 elements and 228 nodes. The mesh is shown in Fig. 5.

The first 6.0 mm of the extrusion process is simulated, where frictionless sliding at contact interfaces is assumed with a linear contact formulation for nodal/elemental penetration. Frictionless sliding is utilized as a simplification since extrusion components are coated with smooth vanadium carbide and the process is well-lubricated. In addition, other research has shown friction values less than 0.1 used in FEA of cold extrusion provide reasonable force-displacement curves and metal flow prediction [85]. Lastly, utilizing linear contact formulation aids in solution convergence as the effects of the die are assumed perfectly rigid.

3. Characterization results

The pre- and post-extrusion grain structures are presented in Fig. 6 using respective grain and IPF maps. The pre-extrusion sample was measured at 1500-times magnification, where the post-extrusion sample was measured at 6000-times magnification. Grains of the pre-extrusion sample are measured in the ED but are assumed representative of the hoop and RD as well due to the nature of annealing homogeneous metal. As shown, the grain structure dramatically changed from relatively large equiaxed structure to highly elongated and ordered with respect to post-extrusion grains. More EBSD scans of the pre- and post-extrusion samples are provided in Appendix A.

The measured initial texture is presented in Fig. 7 in two frames. The initial texture is a $\{111\}$ fiber texture. The experimentally measured texture was compacted from $\sim 10,000$ to 100 weighted crystal orientations to aid in reducing computation duration using the procedure presented in [86-91]. Presented in Fig. 8 is the compacted texture compared to the experimentally measured texture in the hoop direction. As shown, the compacted data is well representative of the original.

Fig. 9 shows optical micrographs of the cross section of the extruded tube. An acid-etching helped better view the interface. While the expected thickness was 527 μ m per layer, 510 μ m was measured for the

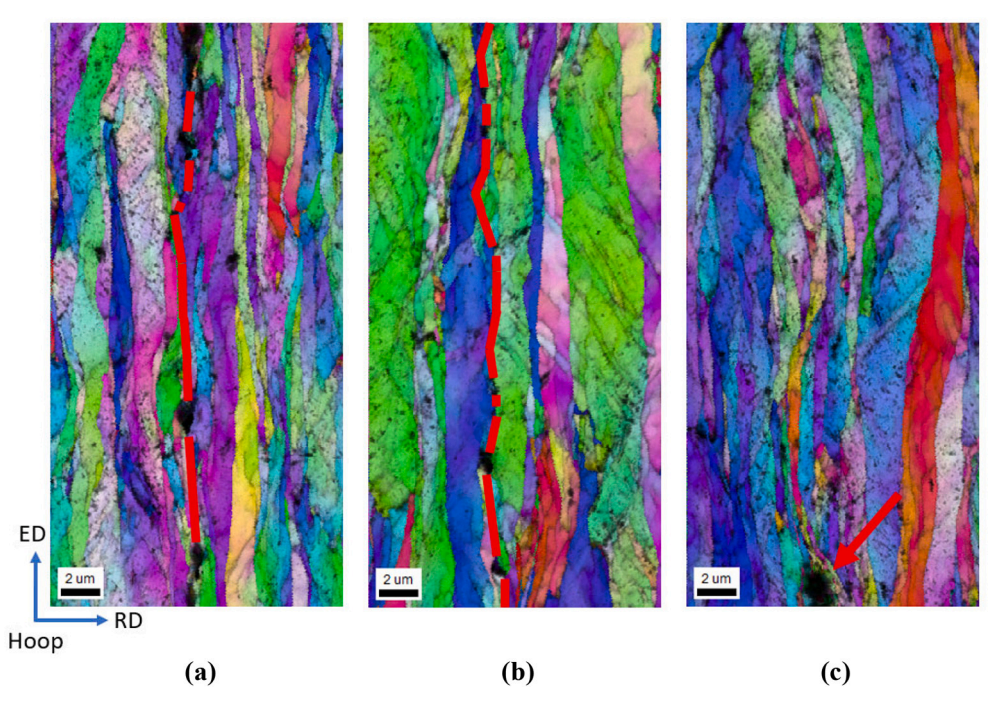


Fig. 10. Three IPF maps of the bond line between the two coextruded Cu tubes. The red line in (a) and (b) highlights the bond line. In (c), the bond line is difficult to determine, however, a void at the interface pointed by the red arrow aids in identification of the bond line. (For interpretation of the references to color in this figure legend, the reader is referred to the web version of this article.)

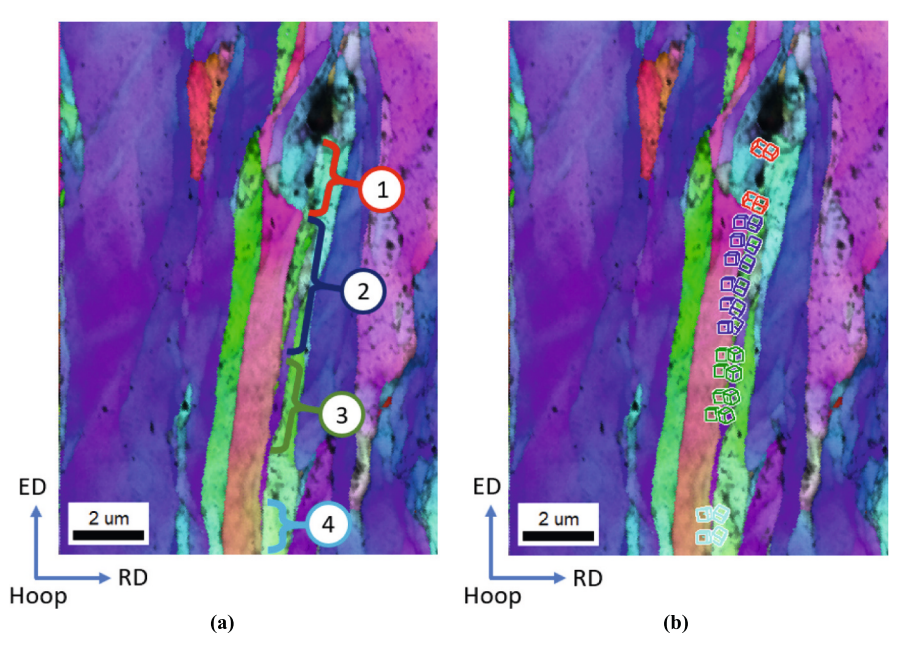


Fig. 11. Of the many Cu—Cu grains that bonded due to 68% AEB, four grain pairs are identified as (1) red, (2) dark blue, (3) green, and (4) cyan. (b) The crystal grain orientations on each side of the bond line are expressed with 3-dimensional cubes at those specific locations along the grain-to-grain bond line. Scans are taken at 12,000-times magnification. (For interpretation of the references to color in this figure legend, the reader is referred to the web version of this article.)

outer layer and 568 μm for the inner layer of copper. Complete bonding did not occur as voids are present at the interface. Voids are black at the interface in the fig. A 15,240 μm long interface was surveyed and \sim 85.0% of the length was found bonded. The voids are expected to collapse during further AEB iterations.

The Cu—Cu bond line is examined using EBSD at 6000-times magnification in lieu of a traditional peel test, which is applicable to rectangular cross-sections. A peel test for multi-layer tubes is yet to be conceived. As shown in Fig. 10, three locations of the bond line are

displayed, where the respective bond lines are highlighted in red in (a) and (b). When voids are not present, it is difficult to ascertain the exact bond line path as seen in (c), where there is a long continuous section of bonding and one void. The identified void indicates the general area of the bond line, but the exact bond line path is too difficult to identify. While globally straight as shown in Fig. 9, the interface is wavy due to local strain accommodation in individual grains and voids. These local effects cause the interface to lose its integrity.

The coupling crystal orientations are examined to the left and right of

Table 2
Euler angles representing crystal orientation sampled along the length of 4 grains bonded using 68% AEB.

| Grain and color reference per Fig. 11 | | Left grain | | | Right grain | | |
|--|-------|------------|-------|----------|-------------|-------|----------|
| | | ϕ_1 | Φ | ϕ_2 | ϕ_1 | Φ | ϕ_2 |
| 1 | Red | 218.2 | 129.4 | 335.8 | 79.9 | 40.1 | 336.5 |
| 1 | Red | 336.4 | 106.7 | 223.1 | 158.8 | 100.0 | 220.4 |
| 2 | Blue | 218.9 | 22.1 | 231.3 | 155.7 | 98.5 | 127.3 |
| 2 | Blue | 179.7 | 106.8 | 165.9 | 60.0 | 129.3 | 262.8 |
| 2 | Blue | 181.0 | 107.4 | 167.3 | 250.3 | 138.9 | 9.0 |
| 2 | Blue | 273.9 | 101.7 | 200.8 | 335.0 | 83.7 | 232.2 |
| 2 | Blue | 31.8 | 156.6 | 209.9 | 66.7 | 35.8 | 352.0 |
| 2 | Blue | 2.2 | 70.7 | 101.7 | 245.2 | 145.4 | 7.9 |
| 3 | Green | 31.4 | 157.9 | 206.5 | 273.3 | 113.5 | 236.9 |
| 3 | Green | 183.5 | 110.4 | 169.7 | 199.9 | 59.6 | 151.6 |
| 3 | Green | 185.8 | 109.8 | 170.4 | 207.0 | 61.7 | 150.8 |
| 3 | Green | 185.8 | 108.5 | 170.3 | 28.4 | 116.0 | 210.3 |
| 4 | Cyan | 186.6 | 113.6 | 174.7 | 331.0 | 81.6 | 235.9 |
| 4 | Cyan | 5.2 | 68.4 | 95.7 | 330.7 | 80.9 | 235.7 |

the Cu—Cu bond line at four different grain-to-grain bonds. As shown in Fig. 11(a), the grain pairs are labelled 1 through 4 and assigned a color. In Fig. 11(b), the grain orientations along the length of the grain-to-grain bonds are represented by 3-dimensional cubes. The characteristic interface that occurs most frequently during ARB of FCC and bodycentered cubic (BCC) metals involves the $\{111\}FCC||\{110\}BCC$ coupling known as the Kurdjumov-Sachs (KS) relationship [92], while

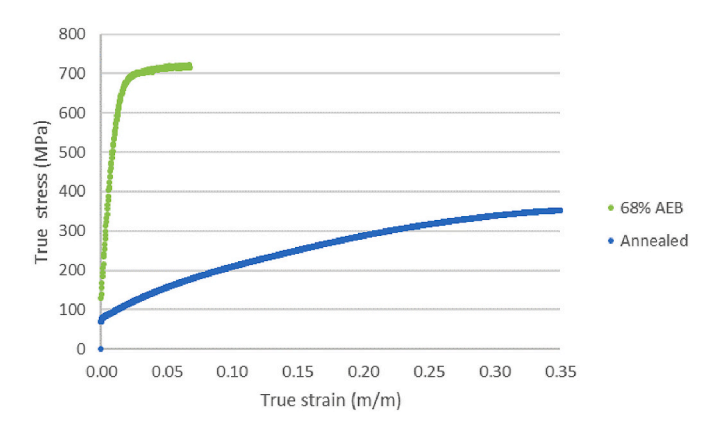


Fig. 13. True stress-strain curve of 68% extruded 2-layer Cu—Cu compared to a corresponding curve of annealed Cu.

for a hexagonal close-packed (HCP)/BCC composite the interfaces involves $\{0001\}$ HCP $||\{110\}$ BCC orientation coupling [93]. Evidently, the FCC-FCC bond line is independent on any specific orientation couplings. As a result, bonding of materials of the same crystal structure may be easier.

The Bunge-Euler angles for these cubes are presented in Table 2. Most notably, for each pair of grain-to-grain bonds, enacted by AEB at room temperature, there is no crystal orientation preference. This is

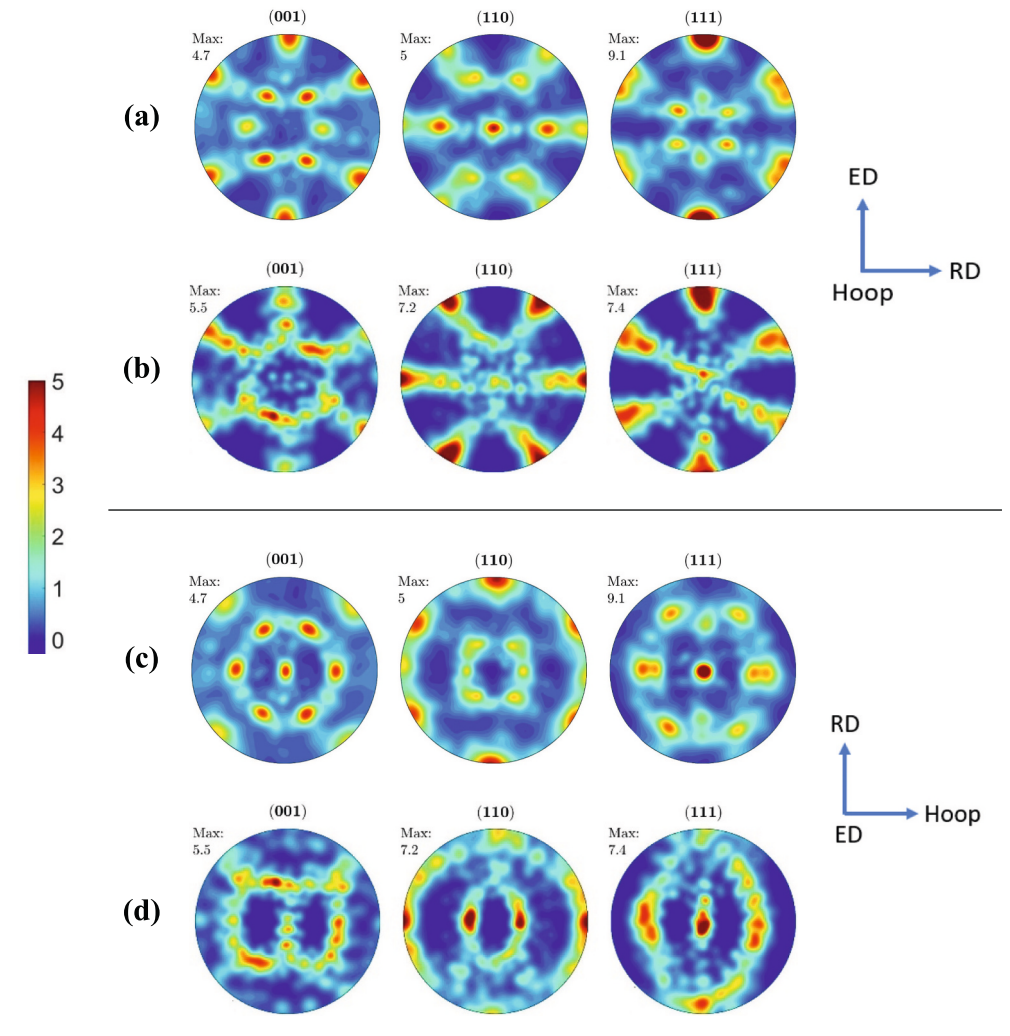


Fig. 12. Pole figures showing texture (a, c) before extrusion and (b, d) after AEB extrusion at 68% deformation in two frames.

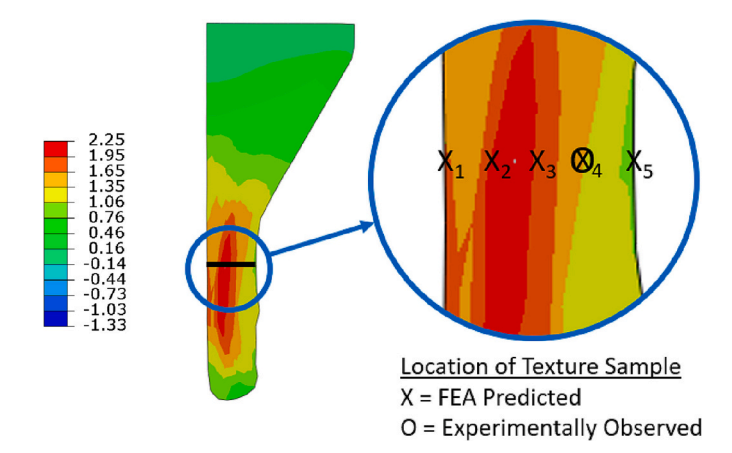


Fig. 14. The FE-EPSC predicted texture is sampled in 5 locations evenly spaced through the extruded wall thickness. The sample locations are overlaid onto the equivalent plastic strain fields. The location 4 coincides with the measuring location.

concluded based on the 14 unique pairs of Euler angles of the respective left and right grain at the bond line. Therefore, this is an example of FCC metal, bonding at room temperature in AEB processing, having no preferential grain orientation when bonded using 68% deformation.

Finally, experimentally measured textures are conducted pre- and post-extrusion to show texture evolution after the extrusion process. As shown in Fig. 12, an extruded or drawn texture featuring {111} fiber is observed. Interestingly, the peak intensity is slightly reduced after AEB. Moreover, the texture evolution during AEB is such that shear texture components slightly increase relative to the initial texture.

In closing the experimental results section, mechanical properties of the extruded material are presented. The Cu—Cu bimetal underwent significant work-hardening during the extrusion at 68% deformation. The hardness after extrusion is 150.7 HK, which is ~168 increase relative to the annealed material. Moreover, the Cu-Cu tube exhibits significantly improved flow strength as shown in Fig. 13. A few tensile tests were performed axially per ASTM E8 using custom sidewall specimens to confirm the results. The 0.2% offset yield strength increased from 83 MPa to 481 MPa. Interestingly, the material still has some residual ductility after the extrusion. The obtained ultimate tensile strength of the Cu-Cu tube is larger than that after ARB [94] and tube cyclic extrusion-compression (TCEC) [95]. The significant improvement in strength can be attributed to the refined and severely elongated grains, their crystallography, and dislocation structures, which are not characterized in the present work. The Cu-Cu tube is expected to exhibit anisotropic material properties as grains and dislocations are not uniform in all spatial directions, but the anisotropy is also not measured in the present work.

4. Simulation results and discussion

The predicted texture from the FE-EPSC model is sampled across the extruded tube wall thickness as shown in Fig. 14. The five texture locations are tactically selected to best represent the texture profile throughout the tube wall, as well as to align one location with the experimentally measured texture location. The experimentally measured texture location corresponds to location X_4 , such that direct comparisons can be made. In Fig. 14, the texture extraction points are overlaid on a contour plot of the plastic equivalent strain field. As shown, there is a strain distribution, and because of this, the texture profile could also change throughout the tube thickness as well. The highest level of equivalent strain occurs nearly at the centerline of the tube wall and dissipates more rapidly to the outer wall rather than the inner wall. The simulation was stopped after 6 mm of extrusion since no further value would be attained once steady state occurs. The sampling

of a profile through the wall thickness, at the onset of steady state extrusion, is the section most relevant for analysis.

The simulated textures, in addition to the experimentally observed textures, are presented in Fig. 15. 7. The location column in Fig. 15 lists the locations shown in Fig. 14. The initial texture is also shown as global over the entire tube after imposing the sample symmetry. The rest are local textures. As shown, the initial experimental local texture moderately evolves to slightly reduce the peak intensity and increase the shear texture components relative to the initial texture. The evolution of texture is a consequence of plastic strain accommodated by crystallographic slip. The pole plots are complemented with a set of twodimensional sections through the orientation space in the appendix for completeness. Fig. 16 shows the predicted strain fields. The predicted strain contours reveal that more shear strain occurs in the outer portion of the tube, while more radial compression is present in the inner portion of the tube. Evidently, the RD strain and ED strain components dominate as the major contributors to the overall plastic strain equivalent. The high negative strain in the RD is expected due to rigid extrusion ledge, as well as the ED strain, which is the necessary strain field to enact tube expansion due to axial extrusion. As a result of heterogeneous strain fields, some spatial gradient in texture is also predicted. However, the major texture components are present at every spatial location.

5. Summary and conclusions

This work described steps involved in a novel accumulative extrusion bonding process aimed at creating ultrafine-laminated structures in metallic tubes. The process was successfully applied to extrusion bond a pure Cu—Cu bimetallic tube at room temperature to facilitate characterization of microstructural evolution and properties. To this end, the work examined the evolution of interface integrity, grain structure, crystallographic texture, and tensile strength after AEB of pure Cu tubes. AEB was simulated using FE-EPSC to understand the evolution of texture during the process. The work is a step forward towards manufacturing ultrafine-laminated structures in metallic tubes. Future works will attempt to manufacture such tubes and to understand bonding mechanisms pursuant of multilayered dissimilar tubes, where bonding mechanisms are unexplored. The main conclusions of the present study are:

- Characterization of the bond line by optical microscopy showed that the interface maintains overall integrity. Given the similarity in grain structure with or without an interface, the presence of voids along the bond line merely facilitated detection of the interface line with SEM/EBSD. A more zoomed-in characterization using SEM/EBSD showed that the interface exhibits a wavy character locally due to grain-scale plasticity. These observations suggest that laminated structures could be achieved with the continuation of the process, but waviness will be present.
- Measuring grain orientations on each side of the bond line using EBSD revealed that bonding FCC to FCC metal using AEB at room temperature produces a steady-state bond independent on coupling grain orientations at the interface. As a result, the role of interface in the evolution of grain structure was secondary.
- A relatively coarse equiaxed grain structure of annealed Cu was converted into a severely elongated grain structure along the extrusion direction after AEB. The conversion of the structure was a consequence of severe axial straining along the ED and compression in RD with some shearing. The axisymmetric strain fields were moderately heterogeneous as driven by die geometry. The shear strain played an important role in forming and as a mechanism aiding the bonding.
- Qualitative observations of texture evolution revealed that an initial texture of Cu tubes evolves to slightly reduce the {111} fiber peak intensity and increase the shear texture components. The process was successfully simulated using FE-EPSC. The simulation of texture

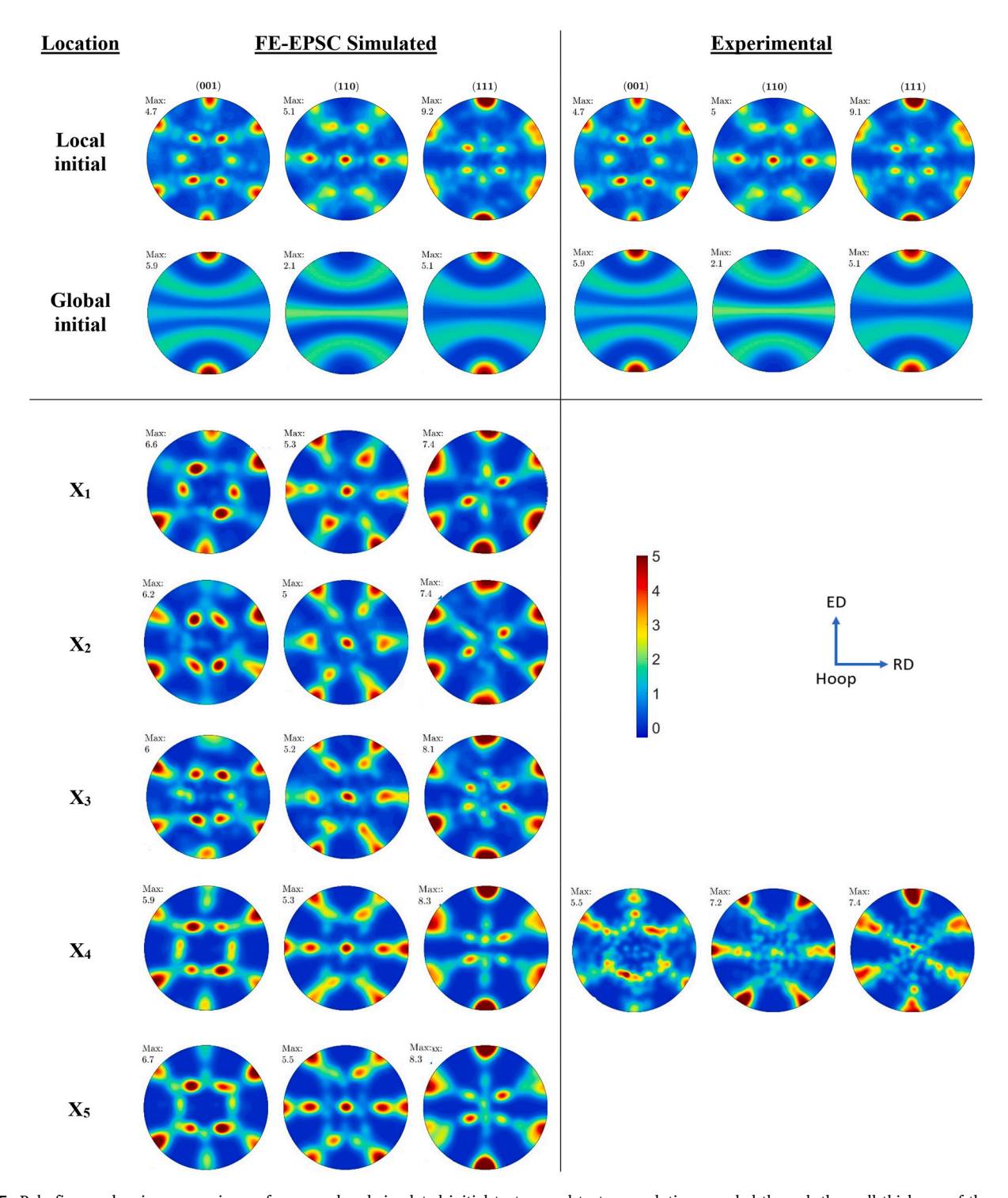


Fig. 15. Pole figures showing comparisons of measured and simulated initial texture and texture evolution sampled through the wall thickness of the extruded copper tube.

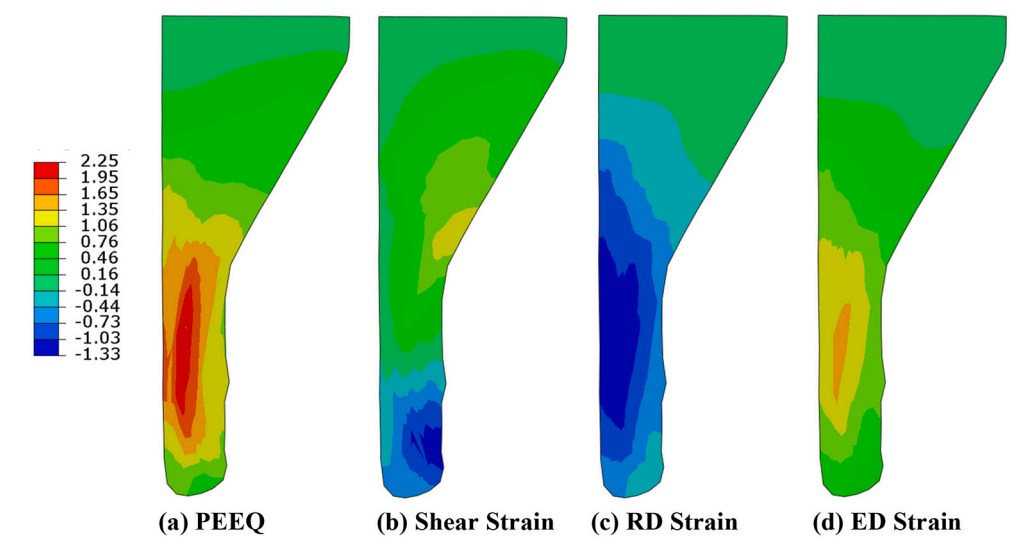


Fig. 16. (a) The equivalent plastic strain (PEEQ) and the logarithmic strain in the (b) shear plane, (c) RD, and (d) ED after 6.0 mm of displacement modeled using FE-EPSC at 68% reduction. The die, punch, and mandrel are omitted.

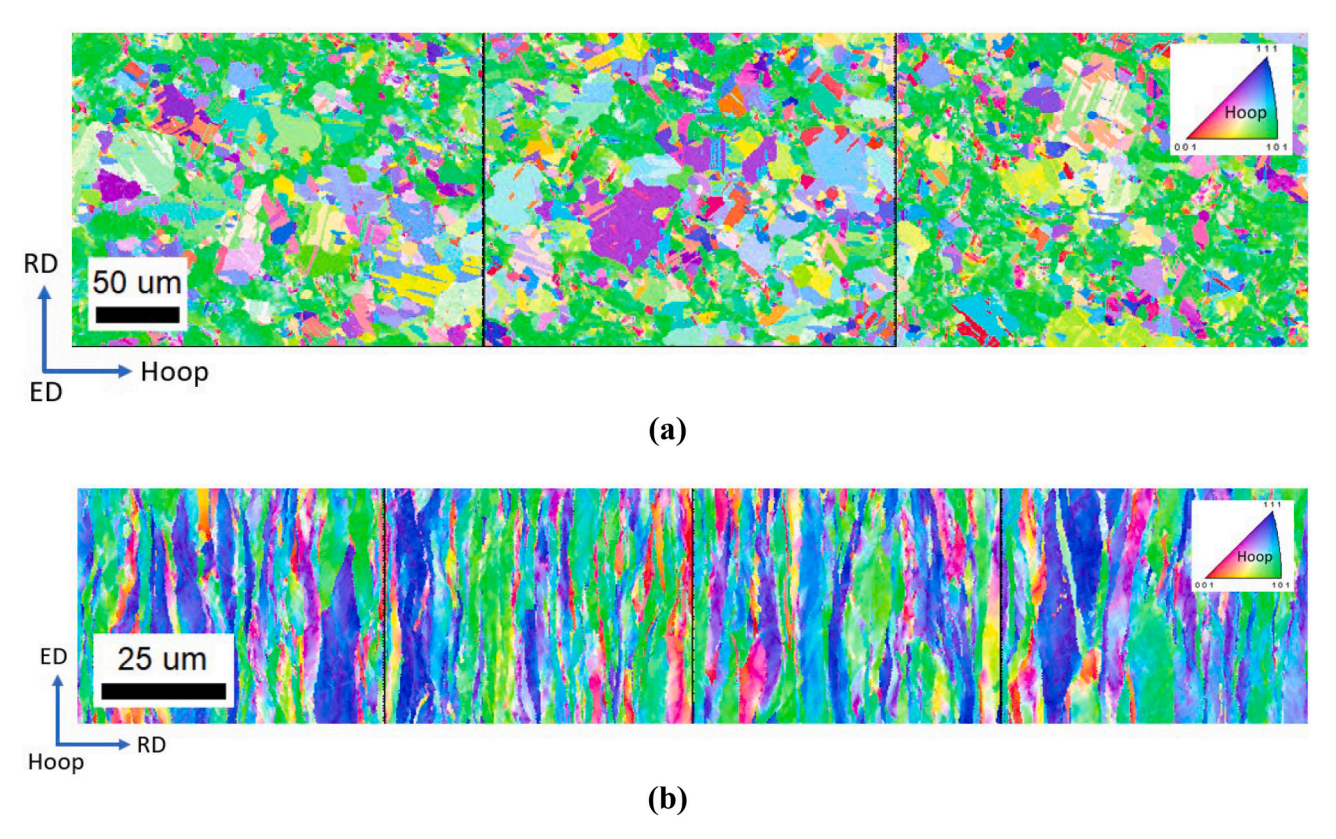


Fig. A1. IPF maps of the (a) annealed pre-extruded and (b) post-extruded copper.

evolution during the process revealed minor gradients in the texture over the through-thickness direction.

• The Cu—Cu bimetal underwent significant work-hardening during the extrusion at 68% reduction. The yield strength of the tube remarkably improved over 5× relative to the annealed material. The significant improvement in strength was attributed to the refined and severely elongated grains, their crystallography, and specific dislocation structures created during AEB.

Declaration of Competing Interest

The authors declare that they have no known competing financial interests or personal relationships that could have appeared to influence the work reported in this paper.

Data availability

The raw/processed data required to reproduce these findings cannot be shared at this time due to technical or time limitations.

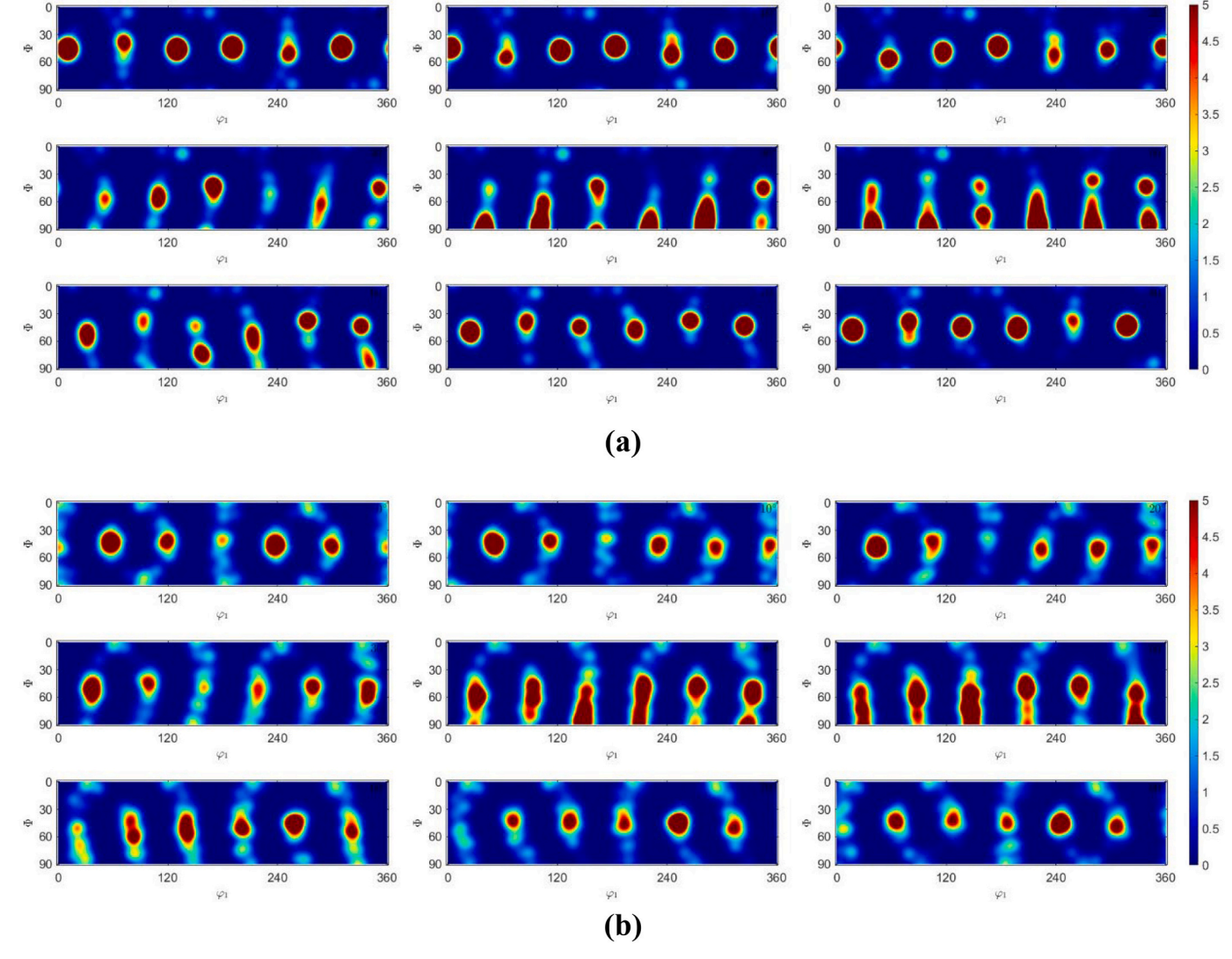


Fig. A2. Comparison of the simulated (a) and measured (b) orientation distributions corresponding to Fig. 15 X_4 as two-dimensional sections through the orientation space in 10^0 increments in φ_2 .

Acknowledgments

This research was accomplished under the CAREER Grant No. CMMI-1650641 funded by the U.S. National Science Foundation.

Appendix A

This appendix presents more EBSD scans in Fig. A1 and two-dimensional sections through the orientation space for X4 row of Fig. 15 in Fig. A2

References

- [1] W.S. Miller, L. Zhuang, J. Bottema, A.J. Wittebrood, P. De Smet, A. Haszler, A. Vieregge, Recent development in aluminium alloys for the automotive industry, Mater. Sci. Eng. A 280 (2000) 37–49.
- [2] J. Hirsch, T. Al-Samman, Superior light metals by texture engineering: optimized aluminum and magnesium alloys for automotive applications, Acta Mater. 61 (2013) 818–843.
- [3] S. Bhowmik, J. Zhang, S.C. Vogel, S.S. Nene, R.S. Mishra, B.A. McWilliams, M. Knezevic, Effects of plasticity-induced martensitic transformation and grain refinement on the evolution of microstructure and mechanical properties of a metastable high entropy alloy, J. Alloys Compd. 891 (2022), 161871.
- [4] M. Bhargava, S. Chakrabarty, V.K. Barnwal, A. Tewari, S.K. Mishra, Effect of microstructure evolution during plastic deformation on the formability of

- Transformation Induced Plasticity and Quenched & Partitioned AHSS, Mater. Des. 152 (2018) 65–77.
- [5] S. Daroju, T. Kuwabara, M. Knezevic, Experimental characterization and crystal plasticity modeling of dual-phase steels subjected to strain path reversals, Mech. Mater. 168 (2022), 104293.
- [6] A.M. Cantara, M. Zecevic, A. Eghtesad, C.M. Poulin, M. Knezevic, Predicting elastic anisotropy of dual-phase steels based on crystal mechanics and microstructure, Int. J. Mech. Sci. 151 (2019) 639–649.
- [7] C.M. Poulin, Y.P. Korkolis, B.L. Kinsey, M. Knezevic, Over five-times improved elongation-to-fracture of dual-phase 1180 steel by continuous-bending-undertension, Mater. Des. 161 (2019) 95–105.
- [8] J. Hirsch, Recent development in aluminium for automotive applications, Trans. Nonferrous Metals Soc. China 24 (2014) 1995–2002.
- [9] S. Daroju, T. Kuwabara, R. Sharma, D.T. Fullwood, M.P. Miles, M. Knezevic, Experimental characterization and crystal plasticity modeling for predicting load reversals in AA6016-T4 and AA7021-T79, Int. J. Plast. 153 (2022), 103292.
- [10] M. Knezevic, C.M. Poulin, X. Zheng, S. Zheng, I.J. Beyerlein, Strengthening of alloy AA6022-T4 by continuous bending under tension, Mater. Sci. Eng. A 758 (2019) 47–55
- [11] E. Hall, The deformation and ageing of mild steel: III discussion of results, Proceedings of the Physical Society. Section B 64 (1951) 747.
- [12] N.J. Petch, The cleavage strength of polycrystals, J. Iron Steel Inst. Lond. 173 (1953) 25–28.
- [13] K. Yaddanapudi, M. Knezevic, S. Mahajan, I.J. Beyerlein, Plasticity and structure evolution of ferrite and martensite in DP 1180 during tension and cyclic bending under tension to large strains, Mater. Sci. Eng. A 820 (2021), 141536.
- [14] N. Sadasivan, M. Balasubramanian, Severe plastic deformation of tubular materials—Process methodology and its influence on mechanical properties—A review, Materials Today: Proceedings 46 (2021) 3460–3468.

- [15] H. Azzeddine, D. Bradai, T. Baudin, T.G. Langdon, Texture evolution in highpressure torsion processing, Prog. Mater. Sci. 125 (2022), 100886.
- [16] M. Jahedi, M.H. Paydar, S. Zheng, I.J. Beyerlein, M. Knezevic, Texture evolution and enhanced grain refinement under high-pressure-double-torsion, Mater. Sci. Eng. A 611 (2014) 29–36.
- [17] M. Jahedi, M. Knezevic, M. Paydar, High-pressure double torsion as a severe plastic deformation process: experimental procedure and finite element modeling, J. Mater. Eng. Perform. 24 (2015) 1471–1482.
- [18] M. Jahedi, I.J. Beyerlein, M.H. Paydar, S. Zheng, T. Xiong, M. Knezevic, Effects of pressure and number of turns on microstructural homogeneity developed in highpressure double torsion, Metall. Mater. Trans. A 48 (2017) 1249–1263.
- [19] M. Jahedi, M.H. Paydar, M. Knezevic, Enhanced microstructural homogeneity in metal-matrix composites developed under high-pressure-double-torsion, Mater. Charact. 104 (2015) 92–100.
- [20] M. Jahedi, E. Ardjmand, M. Knezevic, Microstructure metrics for quantitative assessment of particle size and dispersion: application to metal-matrix composites, Powder Technol. 311 (2017) 226–238.
- [21] G.N.M. Rao, V.R.M. Kumar, A review on recent advances in accumulative roll bonding of similar, dissimilar and metal matrix composites, Materials Today: Proceedings 56 (2021) A13–A18.
- [22] M. Knezevic, T. Nizolek, M. Ardeljan, I.J. Beyerlein, N.A. Mara, T.M. Pollock, Texture evolution in two-phase Zr/Nb lamellar composites during accumulative roll bonding, Int. J. Plast. 57 (2014) 16–28.
- [23] J.S. Carpenter, T. Nizolek, R.J. McCabe, M. Knezevic, S.J. Zheng, B.P. Eftink, J. E. Scott, S.C. Vogel, T.M. Pollock, N.A. Mara, I.J. Beyerlein, Bulk texture evolution of nanolamellar Zr–Nb composites processed via accumulative roll bonding, Acta Mater. 92 (2015) 97–108.
- [24] M. Ardeljan, M. Knezevic, T. Nizolek, I.J. Beyerlein, N.A. Mara, T.M. Pollock, A study of microstructure-driven strain localizations in two-phase polycrystalline HCP/BCC composites using a multi-scale model, Int. J. Plast. 74 (2015) 35–57.
- [25] G. El-Garhy, N. El Mahallawy, M. Shoukry, Effect of grain refining by cyclic extrusion compression (CEC) of Al-6061 and Al-6061/SiC on wear behavior, Journal of Materials Research and Technology 12 (2021) 1886–1897.
- [26] X. Chen, G. Huang, S. Liu, T. Han, B. Jiang, A. Tang, F. Pan, Y. Zhu, Grain refinement and mechanical properties of pure aluminum processed by accumulative extrusion bonding, Trans. Nonferrous Metals Soc. China 29 (2019) 437–447.
- [27] Y. Xin, R. Hong, B. Feng, H. Yu, Y. Wu, Q. Liu, Fabrication of mg/Al multilayer plates using an accumulative extrusion bonding process, Mater. Sci. Eng. A 640 (2015) 210–216.
- [28] A. Azushima, R. Kopp, A. Korhonen, D.-Y. Yang, F. Micari, G. Lahoti, P. Groche, J. Yanagimoto, N. Tsuji, A. Rosochowski, Severe plastic deformation (SPD) processes for metals, CIRP Ann. 57 (2008) 716–735.
- [29] J.A. Muñoz, T. Khelfa, A. Komissarov, J.-M. Cabrera, Ductility and plasticity of ferritic-pearlitic steel after severe plastic deformation, Mater. Sci. Eng. A 805 (2021), 140624.
- [30] D. Lesuer, C. Syn, O. Sherby, J. Wadsworth, J. Lewandowski, W. Hunt, Mechanical behaviour of laminated metal composites, Int. Mater. Rev. 41 (1996) 169–197.
- [31] N.A. Mara, I.J. Beyerlein, Interface-dominant multilayers fabricated by severe plastic deformation: stability under extreme conditions, Curr. Opinion Solid State Mater. Sci. 19 (2015) 265–276.
- [32] B. Clemens, H. Kung, S. Barnett, Structure and strength of multilayers, MRS Bull. 24 (1999) 20–26.
- [33] N. Mara, D. Bhattacharyya, P. Dickerson, R. Hoagland, A. Misra, Deformability of ultrahigh strength 5 nm Cu/ Nb nanolayered composites, Appl. Phys. Lett. 92 (2008), 231901.
- [34] X. Zhang, A. Misra, H. Wang, T. Shen, M. Nastasi, T. Mitchell, J. Hirth, R. Hoagland, J. Embury, Enhanced hardening in cu/330 stainless steel multilayers by nanoscale twinning, Acta Mater. 52 (2004) 995–1002.
- [35] M.R. Standley, M. Knezevic, Towards manufacturing of ultrafine-laminated structures in metallic tubes by accumulative extrusion bonding, Metals 11 (2021) 280
- [36] J. Alcaraz, J. Gil-Sevillano, An analysis of the extrusion of bimetallic tubes by numerical simulation, Int. J. Mech. Sci. 38 (1996) 157–173.
- [37] M. Knezevic, M. Jahedi, Y.P. Korkolis, I.J. Beyerlein, Material-based design of the extrusion of bimetallic tubes, Comput. Mater. Sci. 95 (2014) 63–73.
- [38] L. Kestens, J. Jonas, ASM Handbook, Vol. 14A, Metalworking: Bulk Forming, Materials Park, ASM International, 2005, pp. 685–700.
- [39] V.Y. Mehr, M.R. Toroghinejad, A. Rezaeian, The effects of oxide film and annealing treatment on the bond strength of Al–Cu strips in cold roll bonding process, Mater. Des. 53 (2014) 174–181.
- [40] M. Hosseini, N. Pardis, H.D. Manesh, M. Abbasi, D.-I. Kim, Structural characteristics of Cu/Ti bimetal composite produced by accumulative roll-bonding (ARB), Mater. Des. 113 (2017) 128–136.
- [41] R.N. Dehsorkhi, F. Qods, M. Tajally, Investigation on microstructure and mechanical properties of Al–Zn composite during accumulative roll bonding (ARB) process, Mater. Sci. Eng. A 530 (2011) 63–72.
- [42] L. Ghalandari, M. Mahdavian, M. Reihanian, Microstructure evolution and mechanical properties of Cu/Zn multilayer processed by accumulative roll bonding (ARB), Mater. Sci. Eng. A 593 (2014) 145–152.
- [43] R. Jamaati, M.R. Toroghinejad, Manufacturing of high-strength aluminum/ alumina composite by accumulative roll bonding, Mater. Sci. Eng. A 527 (2010) 4146–4151.
- [44] H. Chang, M. Zheng, C. Xu, G. Fan, H. Brokmeier, K. Wu, Microstructure and mechanical properties of the Mg/Al multilayer fabricated by accumulative roll bonding (ARB) at ambient temperature, Mater. Sci. Eng. A 543 (2012) 249–256.

- [45] M. Mahdavian, L. Ghalandari, M. Reihanian, Accumulative roll bonding of multilayered cu/Zn/Al: an evaluation of microstructure and mechanical properties, Mater. Sci. Eng. A 579 (2013) 99–107.
- [46] D.J. Savage, I.J. Beyerlein, N.A. Mara, S.C. Vogel, R.J. McCabe, M. Knezevic, Microstructure and texture evolution in Mg/Nb layered materials made by accumulative roll bonding, Int. J. Plast. 125 (2020) 1–26.
- [47] M. Ardeljan, M. Knezevic, T. Nizolek, I.J. Beyerlein, N.A. Mara, T.M. Pollock, A study of microstructure-driven strain localizations in two-phase polycrystalline HCP/BCC composites using a multi-scale model, Int. J. Plast. 74 (2015) 35–57.
- [48] M. Ardeljan, I.J. Beyerlein, M. Knezevic, A dislocation density based crystal plasticity finite element model: application to a two-phase polycrystalline HCP/ BCC composites, Journal of the Mechanics and Physics of Solids 66 (2014) 16–31.
- [49] A. Mashhadi, A. Atrian, L. Ghalandari, Mechanical and microstructural investigation of Zn/Sn multilayered composites fabricated by accumulative roll bonding (ARB) process, J. Alloys Compd. 727 (2017) 1314–1323.
- [50] W. Han, A. Misra, N. Mara, T. Germann, J. Baldwin, T. Shimada, S. Luo, Role of interfaces in shock-induced plasticity in Cu/Nb nanolaminates, Philos. Mag. 91 (2011) 4172–4185.
- [51] A. Misra, R. Hoagland, Effects of elevated temperature annealing on the structure and hardness of copper/niobium nanolayered films, J. Mater. Res. 20 (2005) 2046–2054
- [52] A. Bellou, L. Scudiero, D. Bahr, Thermal stability and strength of Mo/Pt multilayered films, J. Mater. Sci. 45 (2010) 354–362.
- [53] Q. Wei, N. Li, N. Mara, M. Nastasi, A. Misra, Suppression of irradiation hardening in nanoscale V/Ag multilayers, Acta Mater. 59 (2011) 6331–6340.
- [54] M. Zhernenkov, M.S. Jablin, A. Misra, M. Nastasi, Y. Wang, M.J. Demkowicz, J. K. Baldwin, J. Majewski, Trapping of implanted He at Cu/Nb interfaces measured by neutron reflectometry, Appl. Phys. Lett. 98 (2011), 241913.
- [55] K. Khaledi, T. Brepols, S. Reese, A multiscale description of bond formation in cold roll bonding considering periodic cracking of thin surface films, Mech. Mater. 137 (2019), 103142.
- [56] K.-I. Mori, N. Bay, L. Fratini, F. Micari, A.E. Tekkaya, Joining by plastic deformation, CIRP Ann. 62 (2013) 673–694.
- [57] K. Khaledi, S. Rezaei, S. Wulfinghoff, S. Reese, A microscale finite element model for joining of metals by large plastic deformations, Comptes Rendus Mécanique 346 (2018) 743–755.
- [58] H. Mohamed, J. Washburn, Mechanism of Solid State Pressure Welding, 1975.
- [59] N. Bay, Cold welding. Part 1: Characteristics, Bonding Mechanisms, Bond Strength, 1986.
- [60] J. Cave, The mechanism of cold pressure welding by rolling, J. Inst. Met. 101 (1973) 203–207.
- [61] Y. Mitani, R. Vargas, M. Zavala, Deformation and diffusion bonding of aluminidecoated steels, Thin Solid Films 111 (1984) 37–42.
- [62] J.M. Parks, Recrystallization welding, Weld. J. (1953) 209–222.
- [63] L. Vaidyanath, M. Nicholas, D. Milner, Pressure welding by rolling, British Welding Jour 6 (1959) 13–28.
- [64] D.B. Dallas, Tool and Manufacturing Engineers Handbook: A Reference Work for Manufacturing Engineers, McGraw-Hill, 1976.
- [65] M. Zecevic, M. Knezevic, Latent hardening within the elasto-plastic self-consistent polycrystal homogenization to enable the prediction of anisotropy of AA6022-T4 sheets, Int. J. Plast. 105 (2018) 141–163.
- [66] M. Zecevic, M. Knezevic, An implicit formulation of the elasto-plastic selfconsistent polycrystal plasticity model and its implementation in implicit finite elements, Mech. Mater. 136 (2019), 103065.
- [67] M. Zecevic, M. Knezevic, Modeling of sheet metal forming based on implicit embedding of the elasto-plastic self-consistent formulation in Shell elements: application to cup drawing of AA6022-T4, JOM 69 (2017) 922–929.
- [68] M. Zecevic, I.J. Beyerlein, M. Knezevic, Coupling elasto-plastic self-consistent crystal plasticity and implicit finite elements: applications to compression, cyclic tension-compression, and bending to large strains, Int. J. Plast. 93 (2017) 187–211.
- [69] M. Knezevic, R.J. McCabe, R.A. Lebensohn, C.N. Tomé, C. Liu, M.L. Lovato, B. Mihaila, Integration of self-consistent polycrystal plasticity with dislocation density based hardening laws within an implicit finite element framework: application to low-symmetry metals, J. Mech. Phys. Solids 61 (2013) 2034–2046.
- [70] M. Zecevic, M. Knezevic, A new visco-plastic self-consistent formulation implicit in dislocation-based hardening within implicit finite elements: application to high strain rate and impact deformation of tantalum, Comput. Methods Appl. Mech. Eng. 341 (2018) 888–916.
- [71] M. Knezevic, I.J. Beyerlein, D.W. Brown, T.A. Sisneros, C.N. Tomé, A polycrystal plasticity model for predicting mechanical response and texture evolution during strain-path changes: application to beryllium, Int. J. Plast. 49 (2013) 185–198.
- [72] M. Knezevic, L. Capolungo, C.N. Tomé, R.A. Lebensohn, D.J. Alexander, B. Mihaila, R.J. McCabe, Anisotropic stress-strain response and microstructure evolution of textured α-uranium, Acta Mater. 60 (2012) 702–715.
- [73] M. Knezevic, I.J. Beyerlein, M.L. Lovato, C.N. Tomé, A.W. Richards, R.J. McCabe, A strain-rate and temperature dependent constitutive model for BCC metals incorporating non-Schmid effects: application to tantalum-tungsten alloys, Int. J. Plast. 62 (2014) 93–104.
- [74] M. Knezevic, I.J. Beyerlein, Multiscale modeling of microstructure-property relationships of polycrystalline metals during Thermo-mechanical deformation, Adv. Eng. Mater. 20 (2018) 1700956.
- [75] M. Knezevic, I.J. Beyerlein, T. Nizolek, N.A. Mara, T.M. Pollock, Anomalous basal slip activity in zirconium under high-strain deformation, Mater. Res. Lett. 1 (2013) 133–140.

- [76] M. Knezevic, J. Crapps, I.J. Beyerlein, D.R. Coughlin, K.D. Clarke, R.J. McCabe, Anisotropic modeling of structural components using embedded crystal plasticity constructive laws within finite elements, Int. J. Mech. Sci. 105 (2016) 227–238.
- [77] M. Knezevic, J.S. Carpenter, M.L. Lovato, R.J. McCabe, Deformation behavior of the cobalt-based superalloy Haynes 25: experimental characterization and crystal plasticity modeling, Acta Mater. 63 (2014) 162–168.
- [78] M. Knezevic, M. Zecevic, I.J. Beyerlein, J.F. Bingert, R.J. McCabe, Strain rate and temperature effects on the selection of primary and secondary slip and twinning systems in HCP Zr, Acta Mater. 88 (2015) 55–73.
- [79] M. Zecevic, Y.P. Korkolis, T. Kuwabara, M. Knezevic, Dual-phase steel sheets under cyclic tension-compression to large strains: experiments and crystal plasticity modeling, J. Mech. Phys. Solids 96 (2016) 65–87.
- [80] M. Zecevic, M. Knezevic, Origins of improved elongation to fracture in cyclic bending under tension of AA6022-T4 sheets as revealed using crystal plasticity modeling, Mech. Mater. 177 (2023), 104546.
- [81] T.J. Barrett, M. Knezevic, Deep drawing simulations using the finite element method embedding a multi-level crystal plasticity constitutive law: experimental verification and sensitivity analysis, Comput. Methods Appl. Mech. Eng. 354 (2019) 245–270.
- [82] M. Zecevic, I.J. Beyerlein, M. Knezevic, Activity of pyramidal I and II <c+a> slip in Mg alloys as revealed by texture development, J. Mech. Phys. Solids 111 (2018) 290–307.
- [83] M. Zecevic, M. Knezevic, B. McWilliams, R.A. Lebensohn, Modeling of the thermomechanical response and texture evolution of WE43 Mg alloy in the dynamic recrystallization regime using a viscoplastic self-consistent formulation, Int. J. Plast. 130 (2020), 102705.
- [84] Z. Feng, S.-Y. Yoon, J.-H. Choi, T.J. Barrett, M. Zecevic, F. Barlat, M. Knezevic, A comparative study between elasto-plastic self-consistent crystal plasticity and anisotropic yield function with distortional hardening formulations for sheet metal forming, Mech. Mater. 148 (2020), 103422.
- [85] A.L. de Moraes Costa, U.S. da Silva, H.S. Valberg, On the friction conditions in FEM simulations of cold extrusion, Procedia Manufacturing 47 (2020) 231–236.

- [86] A. Eghtesad, T.J. Barrett, M. Knezevic, Compact reconstruction of orientation distributions using generalized spherical harmonics to advance large-scale crystal plasticity modeling: verification using cubic, hexagonal, and orthorhombic polycrystals, Acta Mater. 155 (2018) 418–432.
- [87] M. Knezevic, N.W. Landry, Procedures for reducing large datasets of crystal orientations using generalized spherical harmonics, Mech. Mater. 88 (2015) 73–86.
- [88] N. Landry, M. Knezevic, Delineation of first-order elastic property closures for hexagonal metals using fast Fourier transforms, Materials 8 (2015) 6326–6345.
- [89] M. Knezevic, S.R. Kalidindi, Fast computation of first-order elastic-plastic closures for polycrystalline cubic-orthorhombic microstructures, Comput. Mater. Sci. 39 (2007) 643–648.
- [90] T.J. Barrett, A. Eghtesad, R.J. McCabe, B. Clausen, D.W. Brown, S.C. Vogel, M. Knezevic, A generalized spherical harmonics-based procedure for the interpolation of partial datasets of orientation distributions to enable crystal mechanics-based simulations, Materialia 6 (2019), 100328.
- [91] R.E. Marki, K.A. Brindley, R.J. McCabe, M. Knezevic, Crystal mechanics-based thermo-elastic constitutive modeling of orthorhombic uranium using generalized spherical harmonics and first-order bounding theories, J. Nucl. Mater. 560 (2022), 153472.
- [92] N. Mara, I. Beyerlein, Review: effect of bimetal interface structure on the mechanical behavior of Cu–Nb fcc–bcc nanolayered composites, J. Mater. Sci. 49 (2014) 6497–6516.
- [93] M. Ardeljan, M. Knezevic, M. Jain, S. Pathak, A. Kumar, N. Li, N.A. Mara, J. K. Baldwin, I.J. Beyerlein, Room temperature deformation mechanisms of Mg/Nb nanolayered composites, J. Mater. Res. 33 (2018) 1311–1332.
- [94] A. Fattah-Alhosseini, O. Imantalab, Y. Mazaheri, M. Keshavarz, Microstructural evolution, mechanical properties, and strain hardening behavior of ultrafine grained commercial pure copper during the accumulative roll bonding process, Mater. Sci. Eng. A 650 (2016) 8–14.
- [95] A. Babaei, M. Mashhadi, Tubular pure copper grain refining by tube cyclic extrusion–compression (TCEC) as a severe plastic deformation technique, Progress in Natural Science: Materials International 24 (2014) 623–630.